Zhou *et al. Journal of Translational Medicine* (2025) 23:1040
https://doi.org/10.1186/s12967-025-07071-4

Journal of Translational
Medicine

RESEARCH

Open Access

Integrated single-cell RNA-seq analysis reveals that EZH2 regulates the MIF-CD74 axis to modulate T cell activation and exhaustion in hepatocellular carcinoma

Yangyang Zhou[1†], Yi Xu[1†], Mengfan Ye[2†], Jiayi Xing[3], Di Chen[3], AL-Ameer Wail Hussein Ahmed[2], Al-Rahabi Rehab Abdullah Mohammed Ali[2], Chenwei Pan[3*], Xiangchou Yang[2*] and Zan Shen[1*]

Abstract

Background Hepatocellular carcinoma (HCC) is a highly lethal malignancy characterized by a complex pathological mechanism involving multiple genes and progressive stages. The efficacy of targeted and immunotherapy remains limited, highlighting the urgent need for a reliable model to predict prognosis and response to immune checkpoint inhibitors (ICIs).

Methods We developed an integrated model based on genes related to autophagy, senescence, dormancy, mitochondrial function, and tumor stemness. The predictive capability of this model for HCC prognosis and ICI response was evaluated. Single-cell transcriptomic analysis and immunocompetent mouse models were further utilized to elucidate the role of model-associated genes in regulating the tumor immune microenvironment.

Results A 16-gene integrated model was constructed using genes associated with mitochondrial function, autophagy, dormancy, stemness, and senescence. This model demonstrated robust predictive power for HCC prognosis and ICI responsiveness. Single-cell trajectory analysis revealed that EZH2 plays a crucial role in immune cell infiltration, activation, and HCC progression. Additionally, in vivo mouse models further indicated that EZH2 may regulate CD8^{+} T cell activation and exhaustion through the MIF-CD74 signaling pathway.

Conclusion The integrated model holds potential as a prognostic and predictive tool for HCC immunotherapy. EZH2 may influence CD8^{+} T cell activation and exhaustion via the MIF-CD74 axis, providing insights for patient stratification and potential therapeutic strategies to enhance immunotherapy efficacy.

---

†Yangyang Zhou, Yi Xu and Mengfan Ye contributed equally to this work.

*Correspondence:
Chenwei Pan
panchenwei106@163.com
Xiangchou Yang
yangxiangchou@163.com
Zan Shen
sshenzzan@vip.sina.com

Full list of author information is available at the end of the article

Keywords Hepatocellular carcinoma, Integrated model, Single-cell sequencing, Immune response

Introduction

Hepatocellular carcinoma (HCC) is a highly prevalent and lethal malignancy, representing the predominant pathological subtype of primary liver cancer. The majority of HCC patients are diagnosed at an intermediate to advanced stage, often with underlying liver diseases such as viral hepatitis and cirrhosis, which complicate treatment and result in poor prognoses [1]. Although significant progress has been made in surgical interventions, locoregional therapies, targeted therapies, and immunotherapies in recent years, the overall survival of patients with advanced HCC remains limited, and treatment efficacy still needs further improvement [2].

For patients with advanced HCC who are ineligible for surgery or locoregional therapies, a comprehensive treatment approach combining targeted therapy and immunotherapy is commonly employed [3]. Targeted therapy primarily involves tyrosine kinase inhibitors (TKIs) such as sorafenib and lenvatinib; however, fewer than one-third of patients derive clinical benefit from these treatments, and resistance often emerges within six months of initiation [4]. Following the results of the IMbrave150 clinical trial, the combination of the PD-L1 inhibitor atezolizumab and the anti-angiogenic agent bevacizumab has become the first-line treatment for patients with advanced HCC [5, 6]. This regimen has demonstrated superior overall survival and progression-free survival compared to sorafenib. Despite these breakthroughs, the objective response rate remains only 33.2%, highlighting the need to identify patient subgroups most likely to benefit from immune checkpoint inhibitors [6]. Therefore, there is an urgent need to develop reliable models for predicting prognosis and immunotherapeutic responses to advance personalized precision treatment for HCC patients.

Autophagy is a highly conserved cellular process through which cells degrade and recycle damaged and unnecessary proteins, dysfunctional organelles, intracellular pathogens, and stored nutrients [7]. Autophagy plays a dual role in different stages of cancer. In the early stages of tumor development, it acts as a tumor suppressor by maintaining genomic stability, reducing DNA and reactive oxygen species (ROS) damage, inhibiting necrosis and inflammation, and stimulating antitumor immunity [8]. However, during tumor progression and advanced stages, autophagy often facilitates tumor growth, invasion, and metastasis.

Cancer stem cells (CSCs) are a subpopulation of tumor cells with stem cell-like properties, exhibiting both stemness and tumorigenic characteristics. Autophagy is essential for maintaining CSC stemness. It induces various transcription factors involved in CSC self-renewal and tumor aggressiveness, including core stemness regulators such as SOX2 and NANOG [9, 10]. Additionally, autophagy regulates CSC metabolism by providing an alternative energy source under nutrient-deprived conditions [11].

Cellular senescence refers to a state in which cells lose their proliferative capacity in response to intrinsic and extrinsic stressors while retaining metabolic activity [12–14]. Autophagy and senescence share multiple overlapping features, suggesting that they may act cooperatively to protect cells from external stresses, such as radiation and chemotherapy, as well as internal stresses, including telomere shortening and oncogene activation [15]. Autophagy exhibits a dual role in regulating senescence. Initially, it was considered to delay senescence by clearing damaged proteins and organelles. However, subsequent findings indicate that autophagy can also promote senescence by facilitating the synthesis of the senescence-associated secretory phenotype (SASP), particularly in tumor cells [16, 17].

Dormancy refers to a temporary state of metabolic inactivity and proliferative arrest [18]. It serves as a self-protective mechanism that enables cells to withstand unfavorable conditions, stress, or therapeutic interventions such as chemotherapy and radiotherapy. Dormancy is commonly observed in tumor cells, stem cells, and immune cells. In CSCs, oncogene inactivation can induce proliferating tumor cells to enter a dormant state, which is associated with the loss of differentiation potential and/or self-renewal capacity. However, this dormancy is reversible, as tumor cells can regain their self-renewal ability upon oncogene reactivation [19].

The interplay among autophagy, senescence, and dormancy in tumor initiation, progression, and treatment is highly complex. Oncogene inactivation induced by cellular senescence can suppress tumor progression by preventing cancer cell self-renewal. However, it can also lead to tumor dormancy, contributing to tumor evasion, recurrence, and metastasis [20]. In both tumors and the tumor microenvironment, autophagy, senescence, and dormancy exert intricate and dual effects on tumor progression. In the early stages of tumor development, they may suppress tumor growth by limiting cellular damage, preventing uncontrolled proliferation, or eliminating cancerous cells [21]. However, during cancer treatment, these processes often promote tumor progression by enhancing cancer stemness, leading to resistance to chemotherapy and radiotherapy, facilitating immune evasion, or suppressing immune function within the tumor microenvironment [10].The complex interactions among these processes pose significant challenges for cancer therapy while also offering potential therapeutic strategies, such as targeting cancer stem cells through autophagy inhibition, senescence modulation, or dormancy-targeted therapies, as well as regulating the immune microenvironment. However, the precise relationship between autophagy, senescence, dormancy, mitochondrial function, and cancer stemness in hepatocellular carcinoma remains largely unexplored.

Single-cell sequencing enables multidimensional analysis of individual cells at the genomic, transcriptomic, and epigenomic levels, providing more refined biological insights than traditional bulk sequencing [22]. It has significant value in tumor microenvironment (TME) and immunotherapy research. Immune checkpoint inhibitors, such as PD-1/PD-L1 inhibitors, have become essential therapeutic strategies for various cancers. Single-cell sequencing facilitates the characterization of immune cell dynamics within the TME before and after immunotherapy, providing crucial insights for predicting therapeutic responses. Additionally, it can identify gene expression profiles and cellular subtypes associated with immunotherapy efficacy, aiding in the selection of patients more likely to benefit from treatment [23]. Furthermore, single-cell sequencing helps unveil the molecular characteristics of tumor and immune cells, contributing to the discovery of novel tumor immune evasion mechanisms [24].

In this study, we screened and constructed an integrated model based on genes related to autophagy, senescence, dormancy, mitochondrial function, and cancer stemness. We evaluated the model's predictive ability for prognosis and response to immune checkpoint inhibitors in hepatocellular carcinoma patients. Furthermore, through single-cell data analysis and immunocompetent tumor transplantation mouse experiments, we elucidated the role of genes within the model in regulating the tumor immune microenvironment.

Materials and methods

Data source

The sequencing data, single-cell sequencing data, and clinical data were obtained from TCGA (https://www.cancer.gov/tcga/) and GEO (https://www.ncbi.nlm.nih.gov/geo). This study primarily utilized the following databases: TCGA-LIHC ($n=422$, including 50 controls), GSE78220 ($n=28$), GSE166635 (scRNA-seq, 25,189 single-cell transcriptomes from 2 patients) [25], and GSE125449 (19 tumors) [26]. For genes detected by multiple probes, the average expression level was used. Expression data were quantile-normalized after log transformation.

Genes related to autophagy ($n=232$, Human Autophagy Database, autophagy.lu/clustering/index.html) [27, 28], dormancy ($n=11$) [18], mitochondrial function ($n=1136$) [29], senescence ($n=417$, CellAge, https://genomics.senescence.info/cells/) [30], and stemness ($n=21$) [31] were collected from published literature and public databases (Supplementary Table 1).

Model construction and validation

The TCGA-LIHC cohort ($n=422$, including 50 controls) was used as the training set. First, univariate analysis was performed on the hallmark genes related to autophagy, dormancy, mitochondrial function, senescence, and stemness, to identify genes with significant prognostic value for overall survival. Next, multivariate Cox regression analysis was conducted to establish prediction models for each signaling pathway. The integrated model was constructed using the effective genes identified from the aforementioned models ($n=37$). LASSO regression was applied for variable selection and shrinkage by imposing an L1 penalty on the regression coefficients while minimizing the residual sum of squares. Cross-validation was used to determine the optimal λ value.

Comparison with published models

We collected 27 liver cancer prognosis models established using LASSO regression. The risk score was calculated as $\Sigma(\beta i * \mathrm{Exp.i})$, where i represents the number of prognostic genes, βi denotes the coefficient of gene i, and Exp.i represents the expression level of gene i. Receiver operating characteristic (ROC) analysis was performed to compare the integrated model with the 27 published models.

Evaluation of the model's predictive ability for immune checkpoint inhibitor response

The Tumor Immune Dysfunction and Exclusion (TIDE) software (website: http://tide.dfci.harvard.edu/) was used to calculate the tumor TIDE score for predicting the response to immune checkpoint blockade (ICB) therapy [32]. This database was established by integrating data from 188 tumor cohorts, 12 published ICB clinical trials, and 8 CRISPR screening datasets aimed at identifying regulators of lymphocyte-mediated cancer killing and anti-cancer immune responses [33]. The database derives a total score by combining immune dysfunction and immune exclusion scores, which predicts the tumor's response to immune checkpoint inhibitors. A higher TIDE total score typically indicates poorer treatment response and prognosis. TCGA data were used as input to predict immune checkpoint inhibitor responses in the TIDE analysis, and immune response differences between high-risk and low-risk groups in the integrated model were calculated.

Evaluation of immune cell infiltration

Immune cell infiltration in tumor tissues was assessed using the Tumor Immune Estimation Resource (TIMER) (http://timer.cistrome.org/). TIMER utilizes RNA-seq expression data to examine immune cell infiltration in tumor tissues. It provides estimates for the infiltration levels of six immune cell types: B cells, CD4$^+$ T cells, CD8$^+$ T cells, neutrophils, macrophages, and dendritic cells. Additionally, we used CIBERSORT (https://cibersortx.stanford.edu/) to assess immune infiltration in tumor tissues. CIBERSORT is based on the unique gene expression profiles of immune cell types, and it infers the proportions of each cell type by quantifying the similarity between the sample and known reference cell types.

Construction of the nomogram

The nomogram visualizes the relationships between multiple variables. Patient data, including gender, age, grade, TNM stage, and model score, were used as variables. The nomogram was constructed using the "nomogram" function in the "rms" package in R.

Cell pathway and functional enrichment

Gene Set Variation Analysis (GSVA, "GSVA" R package) and Gene Set Enrichment Analysis (GSEA) software were used to compare pathway enrichment differences between high-risk and low-risk groups. The hallmark (H), KEGG (C2), and ontology (C5) gene sets were employed to analyze the differences between the high-risk and low-risk groups.

Single-cell RNA sequencing data analysis

Single-cell RNA sequencing data from public databases GSE166635 and GSE125449 were downloaded from GEO. After quality control, alignment and mapping, cell barcode identification and correction, and estimation of molecular counts using unique molecular identifiers (UMI), a count matrix was generated, representing the estimated number of different molecules produced by each gene in each quantified cell. The data were normalized, and highly variable features were identified and scaled. Cells with low (<200) or high (>5000) feature counts and those with a high percentage of mitochondrial genes ($>15\%$) were removed. Linear dimensionality reduction was performed using PCA to determine the dataset's dimensions. Non-linear dimensionality reduction was done using UMAP or tSNE for better data visualization. Initial cell annotation was conducted using singleR, followed by manual selection of marker genes to finalize cell type annotation. Differentially expressed features between different cell populations (cluster biomarkers) were identified to reveal key gene expression changes. Pseudotime analysis was performed to explore the dynamic changes of cells and reveal the developmental trajectory. Cell-cell interaction relationships were interpreted through cell communication analysis. Functional enrichment analysis was conducted on differentially expressed genes to uncover their potential roles in biological processes.

Cell counting Kit-8 experiment

HCC cells were seeded into a 96-well plate at a density of 2000 to 5000 cells per well. After the cells adhered to the plate, the designated concentrations of drugs were added, and the cells were treated for 3 days. Cell viability was assessed using CCK8, and absorbance was measured at a wavelength of 450 nm according to the manufacturer's instructions.

Animal experiment

EZH2 inhibitor SHR2554 was provided by Jiangsu Hengrui Medicine Co., Ltd. (Jiangsu, China). Hepa1-6 cells (2×10^6 cells per mouse) were injected subcutaneously into the right shoulder of 6-week-old male C57BL/6 immunocompetent mice. The mice were divided into two groups, with 5 mice per group: control group (solvent) and treatment group (treated with SHR2554 at 200 mg/kg daily by oral gavage). Tumor volume was assessed using the modified ellipsoid formula based on caliper measurements: tumor volume $= 1/2 \times$ length $\times$ width^2. When the tumor volume reached approximately 100 mm^3 on average, the mice were randomly assigned to two groups. Tumor volume, body weight, food intake, and overall health status were monitored. If a mouse lost more than 15% of its body weight or failed to thrive, it was euthanized. All mice were housed in a 12-hour light/dark cycle environment with ad libitum access to food and water. After 12 days of treatment, the mice were euthanized, and tumor tissues were harvested. The experiment was conducted with efforts to minimize animal suffering.

Flow cytometry

Tumor tissues from mice were carefully collected to avoid contamination with surrounding normal tissue. The tumor tissue was minced into small pieces and digested with an appropriate amount of collagenase IV solution at 37 °C for 30–60 min with constant shaking. The digest was filtered using a 40 μm cell strainer to obtain a single-cell suspension. The suspension was centrifuged at 800 g for 5 min, and the supernatant was discarded. The pellet was resuspended in FACS buffer. After excluding dead cells using Fixable Viability Dye, a mixture of fluorescent antibodies targeting CD8$^+$ T cells and activation/exhaustion markers was added and incubated on ice for 30 min. Flow cytometry settings were adjusted with appropriate compensation and gating strategies to collect sample data. Data analysis was performed using FlowJo (version 10.8.1) software, including gating and quantification of the expression ratios of activation and exhaustion markers, which were visualized using relevant scatter plots.

Immunohistochemistry and scoring

Tumor tissues from mice were dewaxed and rehydrated, then sectioned. The tissue sections were placed in 0.01 M citrate buffer and subjected to high-temperature pressure heating for antigen retrieval. After blocking with 5% BSA, primary antibodies were applied to cover the entire tissue section, and the sections were incubated in a humidified chamber at 4 °C overnight. After incubation with secondary antibodies, the sections were stained with streptavidin-biotin complex (SABC) working solution and DAB. After dehydration, the tissue sections were mounted using neutral resin.

Immunohistochemistry intensity was graded on a four-level scale: “0” for no staining, “1+” for faint staining visible under high magnification, “2+” for moderate staining between “1+” and “3+” levels, and “3+” for dark staining visible under low magnification. The area of each intensity level was calculated using ImageJ software. The H score was calculated as follows:

$$\text{H score} = 1 \times (\% \text{ of “}1+\text{” area}) + 2 \times (\% \text{ of “}2+\text{” area}) + 3 \times (\% \text{ of “}3+\text{” area}).$$

Antibody information:

Anti-CD74 (abcam, #ab289885).
Anti-EZH2 (abcam, ab283270).
Anti-MIF (STARTER, S-1007-34).
Anti-Ki67 (abcam, ab15580).

Statistical analysis

All statistical analyses were performed using R software (version 4.4.1). The Kaplan-Meier method was used to assess overall survival, and the log-rank test was applied to evaluate the statistical significance of differences. The “timeROC” R package was utilized to estimate the time-dependent receiver operating characteristic (ROC) curves for survival prediction. The waterfall plot was generated using the “maftools” R package. Nomograms were constructed using the “regplot” and “rms” R packages. Single-cell RNA sequencing data analysis was conducted using the “Seurat,” “SingleR,” “inferCNV,” “CellChat,” and “Monocle2” R packages. Pearson’s correlation coefficient (r) was used to assess the correlation between two continuous variables. A P-value of less than 0.05 was considered statistically significant, unless otherwise stated.

Results

Identification of prognosis-related genes and construction of the integrated model

We obtained genes associated with mitochondria, autophagy, dormancy, stemness, and senescence from published literature and public databases. In the TCGA-LIHC dataset, univariate analysis was first performed to exclude genes not significantly associated with prognosis ($P > 0.05$). The remaining genes were then subjected to multivariate Cox regression analysis to construct survival prediction models for each signaling pathway. Additionally, differential expression analysis was conducted, and the expression differences of genes included in the survival prediction models between paired tumor and non-tumor liver tissues were visualized using ridge plots (Fig. 1A–E). Genes that met the criteria of $P < 0.05$ in multivariate Cox regression analysis and exhibited significant differential expression between tumor and non-tumor liver tissues ($P < 0.05$) were selected as candidate genes. These candidate genes were further incorporated into a LASSO regression model to develop the integrated prognostic model.

Evaluation of prognostic models and performance of the integrated model

We conducted time-dependent ROC analysis for each prognostic model. The results showed that the integrated model achieved an AUC > 0.8 at 1, 2, 3, 4, and 5 years, consistently outperforming the prognostic models constructed using genes related to mitochondria, autophagy, dormancy, stemness, and senescence (Fig. 2A). At the 5-year mark, the AUC of the integrated model reached 0.884, while the autophagy- and mitochondria-based models had AUCs between 0.7 and 0.8. In contrast, the dormancy-, senescence-, and stemness-based models exhibited AUCs < 0.7, indicating that the integrated model had the highest predictive accuracy (Fig. 2B). Additionally, in the time-dependent ROC analysis of the integrated model, the AUC increased over time, suggesting an improvement in prediction accuracy with longer follow-up (Fig. 2C).

The integrated model was composed of 16 genes, including six mitochondria-related genes (GOT2, RP8, TIMM23, TIMMDC1, MUYTH, and RAB5IF), four autophagy-related genes (HSPA8, HSP90AB1, RELA, and RAB7A), four senescence-related genes (MCRS1, FANCD2, ASF1A, and STK32C), and two stemness-related genes (EZH2 and BMI1). Correlation analysis of mRNA expression levels revealed a strong positive correlation between EZH2 and FANCD2, as well as between TIMMDC1 and RAB7A. Conversely, GOT2 showed a negative correlation with HSPA8 and HSP90AB1 (Fig. 2D). Furthermore, we assessed the correlation between the integrated model score and the scores of other models, demonstrating the highest correlation with the mitochondria- and senescence-based models (Fig. 2E).

Subsequently, we performed prognostic analyses for all models. Kaplan–Meier survival curves indicated that the integrated model provided superior prognostic stratification for HCC patients compared to models based on mitochondria, autophagy, dormancy, stemness,

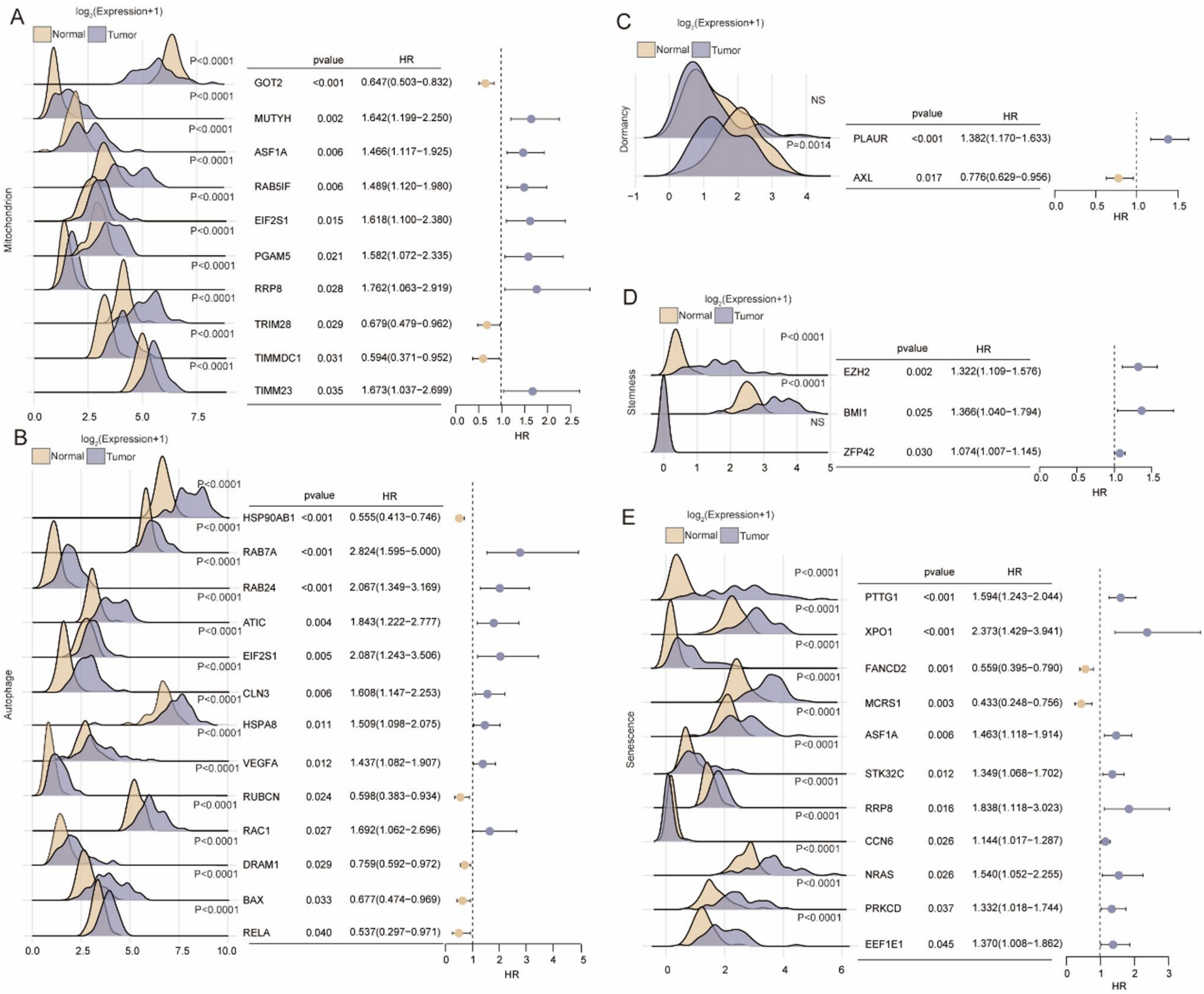

Fig. 1 Differential expression analysis of paired liver cancer tumor tissues and non-tumor liver tissues in the TCGA liver cancer database, along with multivariable Cox regression analysis, illustrates the prognostic significance of genes from each model in liver cancer. We constructed prognostic models based on mitochondrial (**A**), autophagy (**B**), dormancy (**C**), stemness (**D**), and aging (**E**) genes. Differential expression of genes between liver cancer tumor tissues and non-tumor liver tissues was determined using paired t-tests and presented as peak plots. The hazard ratios are shown in the forest plot

or senescence-related genes (Fig. 2F). Additionally, we reviewed 27 published LASSO-based prognostic models for HCC and found that our integrated model achieved the highest 5-year AUC, further confirming its predictive accuracy (Fig. 2G and Supplementary Table 2). Collectively, these results demonstrate that the integrated model, based on mitochondria-, autophagy-, dormancy-, stemness-, and senescence-related genes, offers superior prognostic capability for HCC.

Association between the integrated model, immune infiltration, and immunotherapy response

To investigate the relationship between the integrated model and immune infiltration, we analyzed the correlation between the risk scores of the integrated model and 50 immune checkpoints and regulatory molecules. The results indicated a strong association between the integrated model score and various immune-related ligands, receptors, and co-stimulators, suggesting potential immunological relevance (Fig. 3A). Enrichment analysis further revealed differences in the immune microenvironment between high- and low-risk groups. Specifically, Hallmark enrichment analysis indicated significant enrichment of inflammatory response pathways in the high-risk group, while KEGG analysis showed enrichment of immune networks for IgA production. Additionally, GO analysis revealed significant enrichment of adaptive immune response (GO BP), immunoglobulin complex (GO CC), and antigen binding (GO MF) in the high-risk group (Supplementary Fig. 1).

To preliminarily explore immune infiltration differences between the high-risk (integrated model score ≥ median)

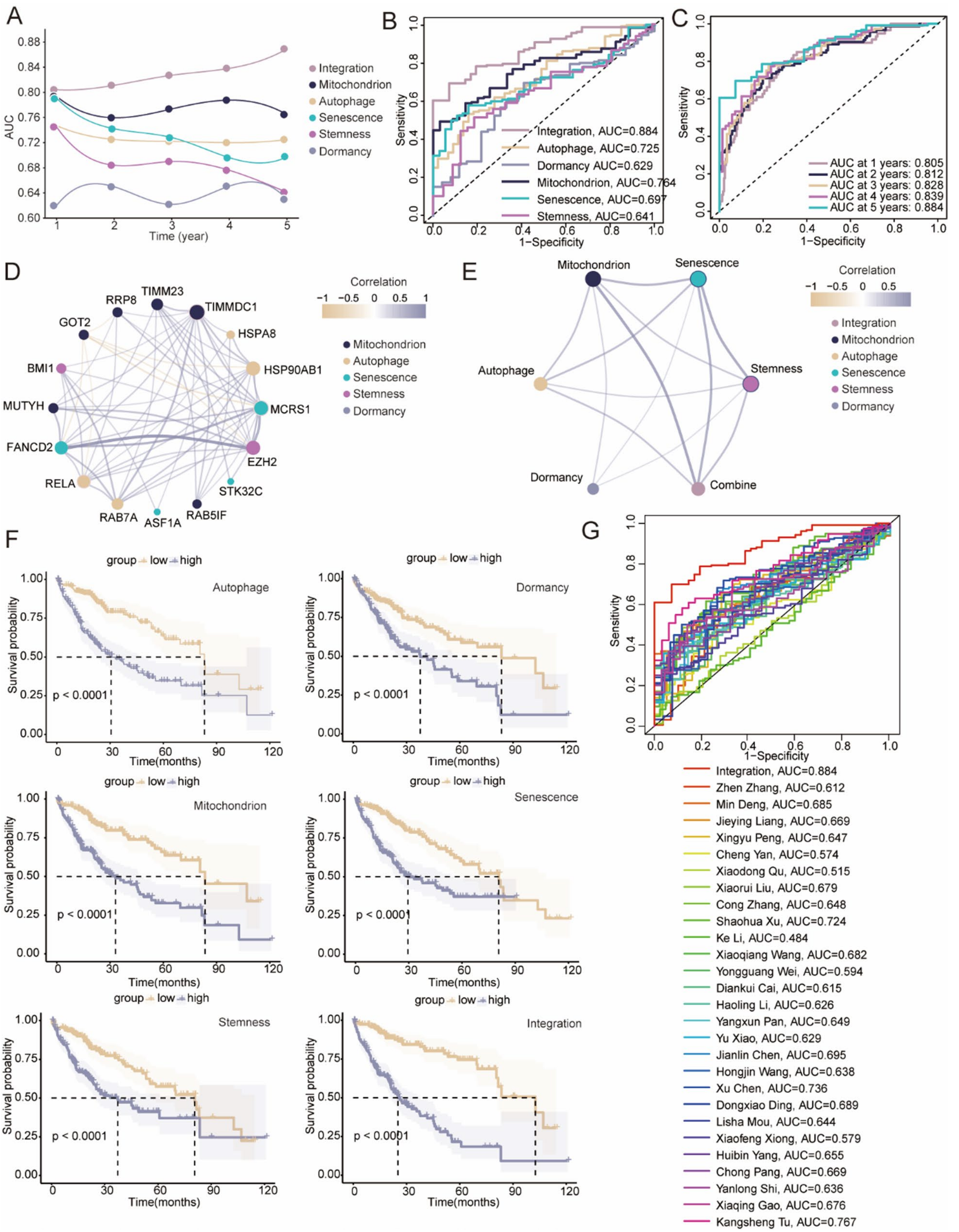

Fig. 2 (See legend on next page.)

(See figure on previous page.)

Fig. 2 Evaluation of the performance of six prognostic models. **A** Area under the receiver operating characteristic (ROC) curve for the six prognostic models at 1, 2, 3, 4, and 5 years. **B** ROC curves of the six prognostic models. **C** Time-dependent ROC curves for the Integrated model. **D** Correlation analysis showing the associations between genes in the Integrated model and their respective model origins. **E** Correlation analysis showing the associations between the six models. **F** Kaplan-Meier survival curve analysis demonstrating prognostic differences between high-risk and low-risk groups for the six models. The survival curves are shown with 95% confidence intervals and analyzed by log-rank test. **G** ROC curves showing the AUC of the Integrated model and 27 published liver cancer prognostic models

and low-risk (integrated model score < median) groups, we used TIMER to predict the infiltration levels of six immune cell types, including B cells, $CD4^+$ T cells, $CD8^+$ T cells, neutrophils, macrophages, and dendritic cells. The results showed that the high-risk group exhibited significantly higher infiltration levels of all six immune cell types (Fig. 3B). Furthermore, we applied CIBERSORT to assess the correlation between gene expression in the integrated model and the infiltration proportions of 18 immune cell types in the tumor microenvironment. The top six immune cells showing the strongest correlation with the integrated score are presented in Fig. 3C, D.

The Tumor Immune Dysfunction and Exclusion (TIDE) algorithm was utilized to evaluate the response of TCGA-LIHC patients to immune checkpoint blockade (ICB) therapy. This model categorizes patients as responders (TIDE score < 0) or non-responders (TIDE score ≥ 0) (Fig. 3E). Patients in the high-risk group exhibited significantly higher TIDE scores, indicating a greater likelihood of non-response to immune checkpoint inhibitors (Fig. 3F, G).

Additionally, we applied the integrated model to other cancer cohorts. Although GSE78220 is a melanoma cohort, both melanoma and HCC are considered immunogenic tumors with shared immune features, such as T cell exhaustion and immune checkpoint expression patterns. Therefore, the use of GSE78220 provides a relevant immunological context for validating immune-related predictive signatures [34, 35]. In the melanoma cohort (GSE78220), patients in the high-risk group (integrated score ≥ median) demonstrated a lower response rate to anti-PD-1 therapy compared to the low-risk group (38.46% vs. 66.67%) (Fig. 3H). Moreover, the prognosis of high-risk patients was significantly worse than that of low-risk patients ($P = 0.022$) (Fig. 3I).

In summary, patients in the high-risk group exhibited lower response rates to immune checkpoint inhibitors, suggesting that the integrated model score may serve as a predictive biomarker for immunotherapy sensitivity.

Genetic alterations in the integrated model and construction of the nomogram model

We systematically analyzed the copy number variation (CNV) frequency of gene gains and losses for the 16 genes included in the integrated model. Among them, nine genes (HSP90AB1, EZH2, FANCD2, RRP8, TIMM23, RAB7A, MCRS1, BMI1, and RAB5IF) exhibited a higher frequency of CNV gains than losses, whereas the remaining seven genes (STK32C, MUTYH, RELA, GOT2, ASF1A, HSPA8, and TIMMDC1) showed a higher frequency of gene loss (Fig. 4A). A Circos plot illustrated that these 16 genes are distributed across multiple chromosomes (Fig. 4B).

The waterfall plot revealed that patients in the low-risk group exhibited a higher mutation rate in TTN and CTNNB1, whereas the high-risk group showed higher mutation rates in TP53 and ABCA13 (Fig. 4C, D). To further enhance the clinical utility of the integrated model, we constructed a nomogram model incorporating the integrated risk score along with clinical and pathological features in the study cohort. Variables including sex, age, tumor grade, TNM staging, and risk score were assigned values ranging from 0 to 100. The sum of these values generated a total score, which can be used to predict patient prognosis (Fig. 4E–G).

Single-cell sequencing analysis

The previous analyses were based on bulk transcriptomic data, which represent mixed information from various cell populations but lack the resolution to delineate the cellular diversity within the TME at the single-cell level. To address this limitation, we leveraged single-cell RNA sequencing (scRNA-seq) data from liver cancer tissues to investigate the role of the genes in the integrated model in both liver cancer cells and immune-infiltrating cells.

We retrieved single-cell sequencing datasets GSE166635 and GSE125449 from the GEO database, where GSE166635 served as the training dataset, and GSE125449 was used for validation. After a multi-step quality control and filtering process, we performed cell-type annotation based on marker genes. In GSE166635, cells were classified into eight subpopulations, including endothelial cells, hepatocytes, liver cancer cells, Kupffer cells, macrophages, T cells, $CD8^+$ T cells, and exhausted $CD8^+$ T cells (Fig. 5A, B). In GSE125449, an additional $CD4^+$ T cell cluster was identified, leading to a total of nine cell populations (Supplementary Fig. 2A, B). We then analyzed the differential expression of the 16 genes in the integrated model across different cell subpopulations and visualized the top three genes with the most significant differential expression using UMAP plots (Fig. 5C and Supplementary Fig. 2C). To further characterize chromosomal alterations in liver cancer cells, we employed InferCNV to identify large-scale copy number

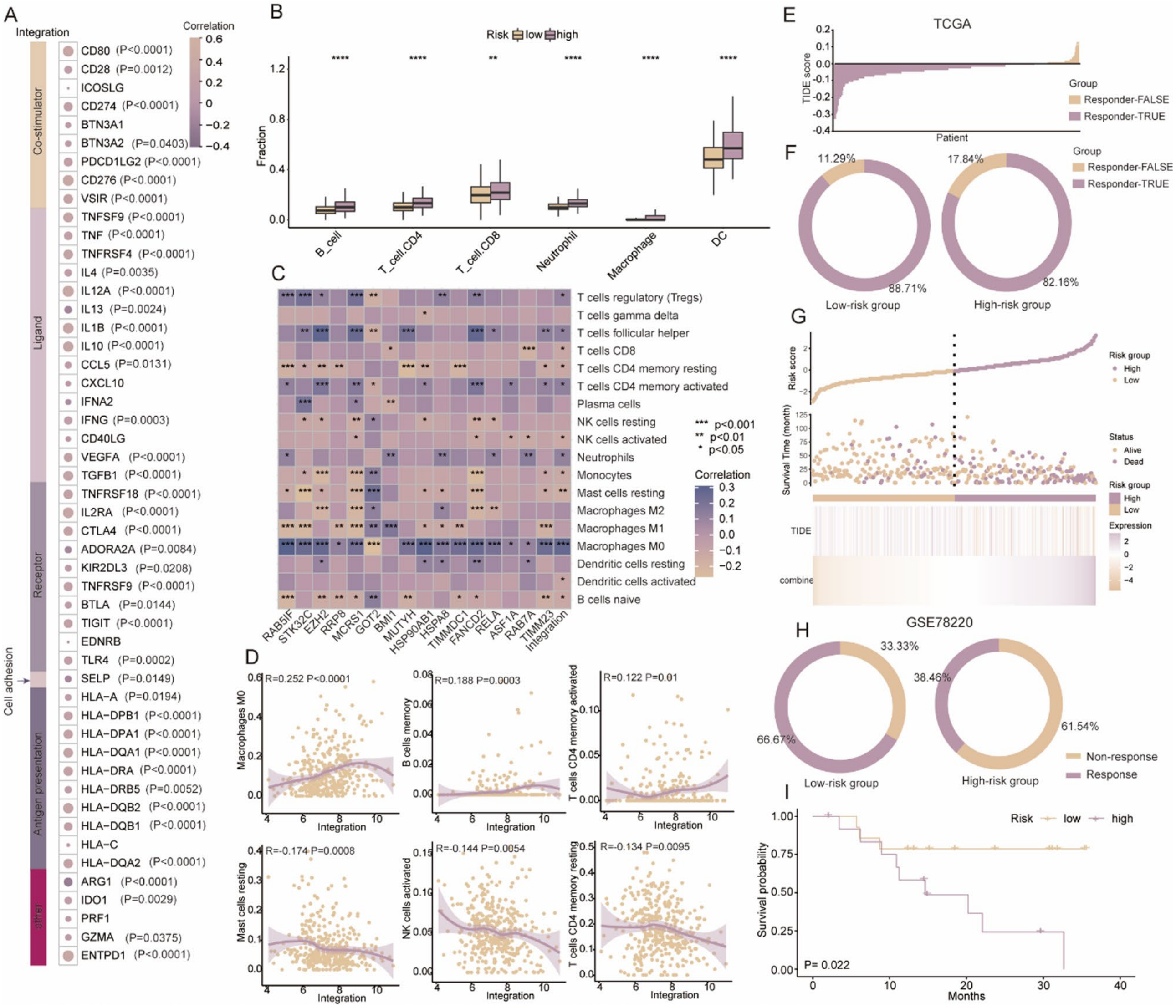

Fig. 3 Comparison of immune treatment efficacy between high-risk and low-risk groups defined by the Integrated model. **A** Correlation heatmap between Integrated score and immune checkpoints. The size of the dots represents the absolute value of the correlation. **B** Significant differences in immune cell infiltration between high-risk and low-risk groups based on the Integrated model. **C** Correlation between gene expression and immune cell infiltration in the Integrated model, as well as the Integrated score. **D** Scatter plot showing the correlation between Integrated score and significantly different immune cell infiltration. **E** Tumor Immune Dysfunction and Exclusion (TIDE) analysis indicating the distribution of patients responding and non-responding to immune checkpoint inhibitors. **F** Percentage of immune checkpoint inhibitor responders in the low-risk group compared to the high-risk group. **G** Distribution of TIDE, survival time, and Integrated score. **H** Differential response to immune checkpoint inhibitors in the high-risk and low-risk groups from the GSE78220 database. **I** Kaplan-Meier survival curve analysis of the high-risk and low-risk groups based on Integrated score. The high-risk group is defined as having an Integrated score ≥ median value, while the low-risk group has an Integrated score < median value

variations (CNVs) in the single-cell sequencing data, using endothelial cells as a reference. The results indicated that liver cancer cells exhibited higher CNV levels than hepatocytes, reinforcing the malignant nature of the identified liver cancer cells (Fig. 5D). Consistently, InferCNV analysis demonstrated that most model genes in malignant hepatocytes exhibited expression trends matching their CNV status, with CNV gains (EZH2, RAB5IF, RRP8, BMI1) corresponding to higher transcript levels and CNV losses (GOT2, TIMMDC1) to lower levels.

Dynamic changes in integrated model genes during cellular transition

To explore whether the genes in the integrated model contribute to cell fate decisions during immune cell activation and liver cancer cell evolution, we constructed single-cell trajectories. Our analysis revealed that during the transition from hepatocytes (red) to liver cancer

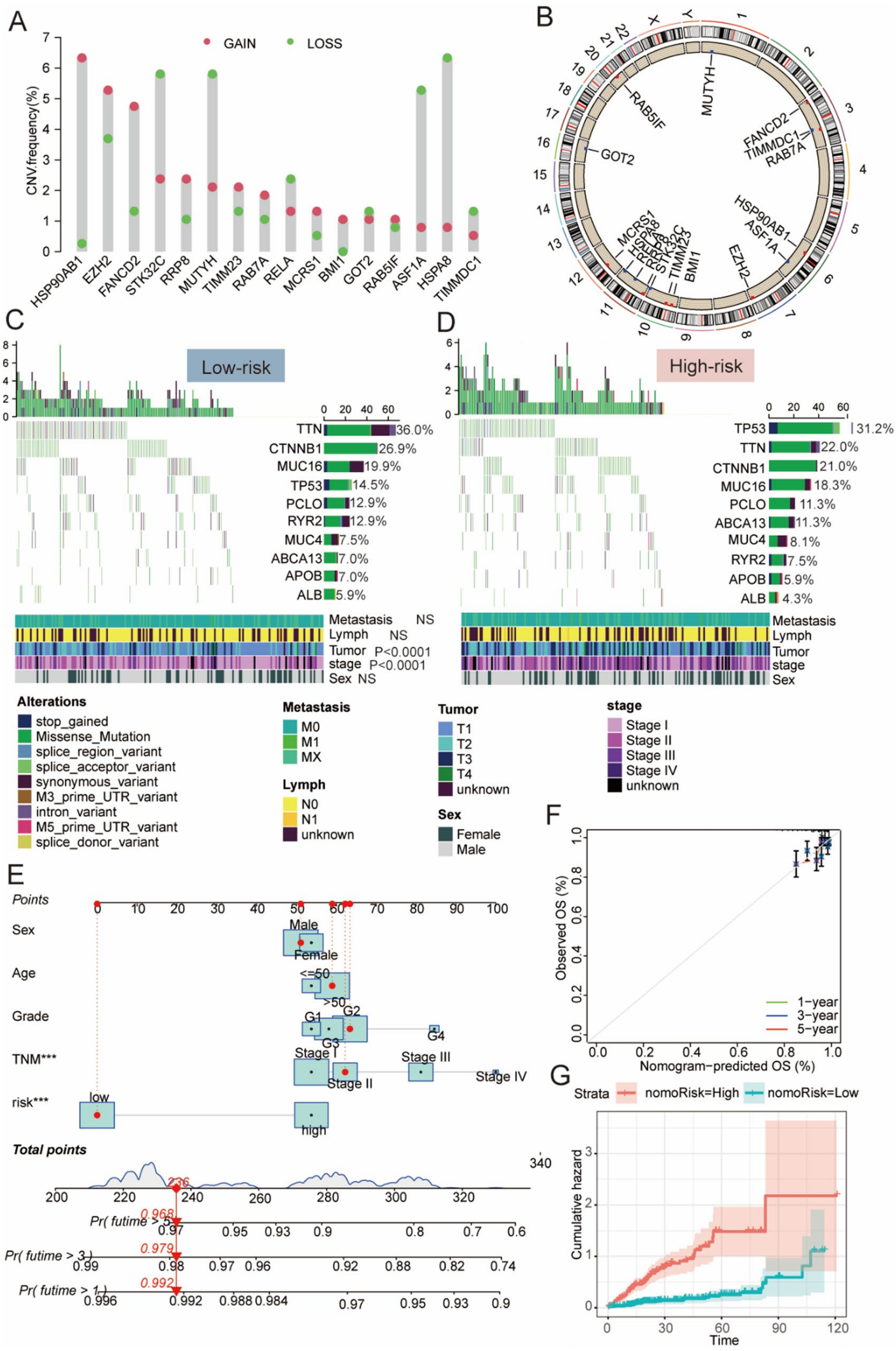

Fig. 4 Genetic abnormalities of genes in the integrated scoring model. **A** Frequency of copy number variations (CNV) in the 16 genes identified in the scoring model. **B** Circos plot showing the chromosomal locations of the 16 genes identified in the model. **C**, **D** Waterfall plots displaying the somatic mutation frequency and differences in clinical information for the low-risk group (**C**) and high-risk group (**D**) patients. **E**–**G** Nomogram prediction model for liver cancer patients showing survival probability (**E**), calibration curve (**F**), and cumulative risk (**G**)

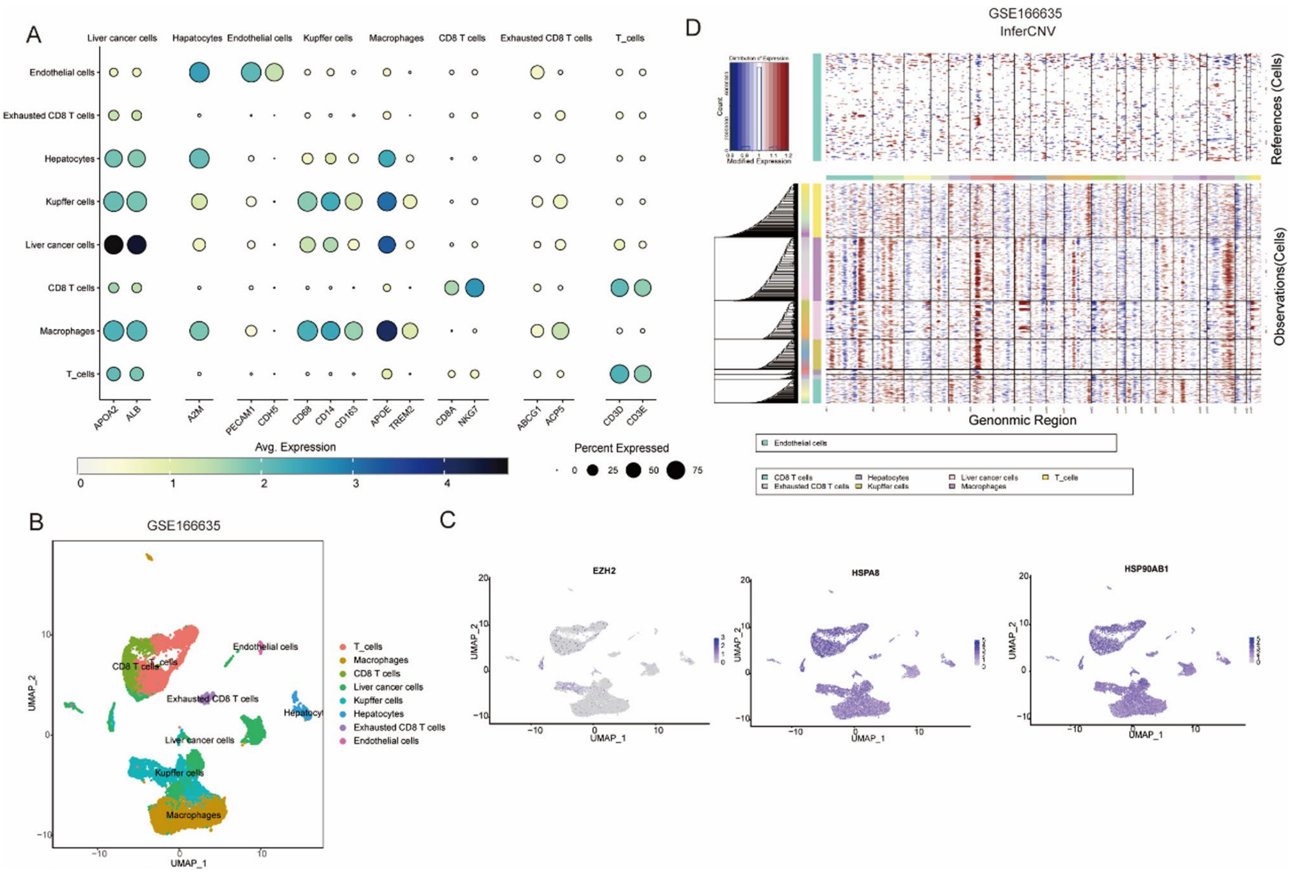

Fig. 5 **A** Bubble plot showing the expression of 16 marker genes across 8 cell types. The size of the bubbles represents the proportion of cells expressing the gene, and the color gradient indicates the average expression level of the marker genes. **B** UMAP plot displaying the major cell types identified in the training cohort GSE166635. **C** UMAP highlighting the top differentially expressed in various cell types from the model. **D** InferCNV heatmap displaying the relative expression intensity across each chromosome. The red regions indicate an increase in gene copy number, while the blue regions show a decrease in gene copy number. The upper half of the heatmap generally displays expression from reference cells (endothelial cells), while the lower half shows expression from other tested cells

cells (green), the expression level of EZH2 exhibited a dynamic increase during tumor differentiation in both GSE166635 and GSE125449 (Fig. 6A, B, Supplementary Fig. 2D). This suggests that these genes may play a role in determining the fate of tumor cells. Furthermore, in liver cancer tissues, CD8$^+$ T cells undergoing exhaustion showed elevated expression of HSP90AB1 (Fig. 6C, D, Supplementary Fig. 2E). Additionally, during the differentiation of Kupffer cells, we observed dynamic change in EZH2 expression (Fig. 6E, F, Supplementary Fig. 2F). These findings indicate that specific genes in the integrated model are dynamically regulated during cancer progression and immune cell exhaustion, highlighting their potential roles in tumor evolution and immune modulation.

Role of EZH2 in the fate determination of liver cancer cells

Given the functional significance of EZH2 in both liver cancer cells and immune cells, we stratified cell subpopulations into high- and low-EZH2 expression groups based on the median EZH2 expression level. Through differential expression analysis, we identified significantly differentially expressed genes across various cell subpopulations (Fig. 7A). UMAP visualization indicated that EZH2 expression was predominantly enriched in Kupffer cells and liver cancer cells (Fig. 7B). To further investigate the intercellular communication between liver cancer cells and other cell types, we analyzed ligand-receptor interactions. Our results revealed that the MIF-CD74 signaling axis was the most significant ligand-receptor interaction between liver cancer cells and other cells (Fig. 7C, Supplementary Fig. 3A). Hierarchical clustering analysis demonstrated that liver cancer cells had strong interactions with exhausted CD8$^+$ T cells, CD8$^+$ T cells, and Kupffer cells (Fig. 7D, Supplementary Fig. 3B).

Since the MIF signaling pathway emerged as the key intercellular communication axis, we examined the expression of critical genes in this pathway across different cell populations. MIF was predominantly expressed in liver cancer cells, while CD44 and CXCR4 were highly

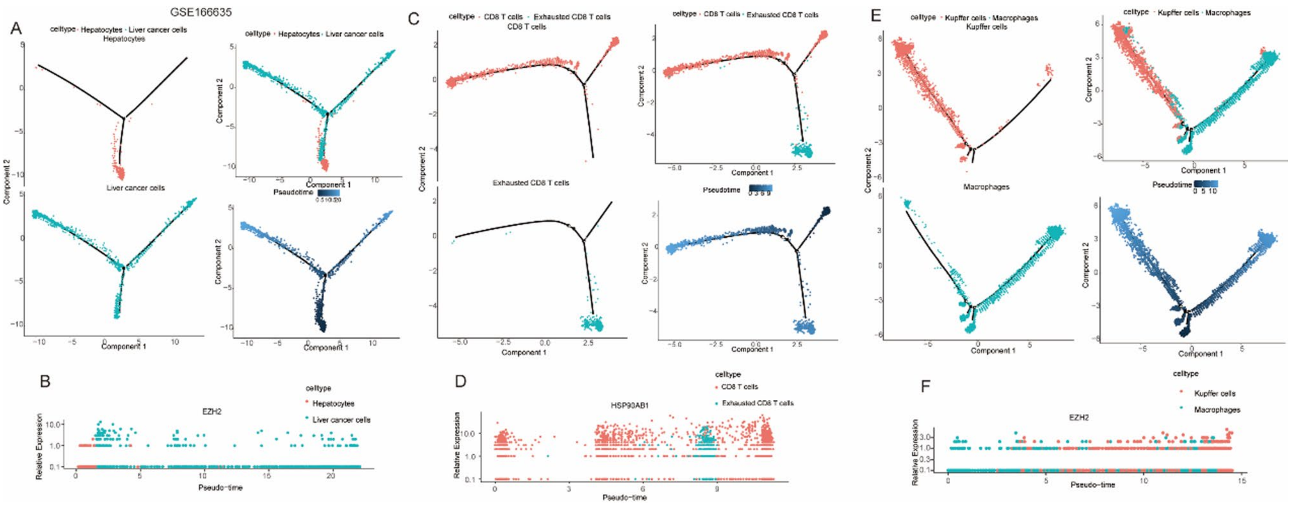

Fig. 6 Pseudotime analysis of cell types and dynamic expression trajectories of Integrated model genes in the training cohort. **A**, **C**, **E** Single-cell motility trajectories for liver cancer cells and hepatocytes (**A**), CD8 T cells and exhausted CD8 T cells (**C**), and Kupffer cells and macrophages (**E**). **B**, **D**, **F** The top dynamic genes during cell differentiation for liver cancer cells and hepatocytes (**B**), CD8 T cells and exhausted CD8 T cells (**D**), and Kupffer cells and macrophages (**F**)

expressed in exhausted $CD8^+$ T cells and $CD8^+$ T cells. Additionally, CD74 was mainly expressed in exhausted $CD8^+$ T cells, Kupffer cells, and macrophages, providing a theoretical basis for the regulation of the tumor microenvironment by liver cancer cells through the MIF-CD74/CD44/CXCR4 signaling axis (Fig. 7E, Supplementary Fig. 3C). Furthermore, our cell-cell communication analysis indicated that cells with high EZH2 expression exhibited a greater number and stronger intensity of intercellular interactions compared to those with low EZH2 expression (Fig. 7F, Supplementary Fig. 3D). Circular plots further visualized the quantitative and qualitative differences in intercellular communication between high- and low-EZH2 expression groups (Fig. 7G, H, Supplementary Fig. 3E). These findings suggest that liver cancer cells may modulate the tumor microenvironment through EZH2-mediated regulation of the MIF signaling axis, thereby influencing immune cell interactions and tumor progression.

EZH2 regulates $CD8^+$ T cell activation and exhaustion via the MIF-CD74 axis

To investigate how EZH2 influences $CD8^+$ T cells through the MIF-CD74 signaling axis, we first examined the effects of the EZH2 inhibitor SHR2554 on liver cancer cells at the cellular level. Our results showed that SHR2554 exhibited a more pronounced inhibitory effect on the murine liver cancer cell line Hepa1-6 compared to human liver cancer cell lines SNU449, PLC/PRF/5, and MHCC97H (Fig. 8A). To further explore how EZH2 inhibition affects $CD8^+$ T cells, we established a C57BL/6 immunocompetent mouse model of liver cancer and divided the mice into two groups, treated with vehicle or SHR2554. The results demonstrated that treatment with 200 mg/kg/day of SHR2554 significantly suppressed tumor volume without affecting body weight (Fig. 8B–E). EZH2 inhibition promoted $CD8^+$ T cell activation, as evidenced by an increase in the production of IFN-γ and Granzyme B (GranB) (Fig. 8F). These findings suggest that tumor-derived EZH2 may negatively regulate $CD8^+$ T cell activation. Interestingly, we also observed that EZH2 inhibition significantly reduced the frequency of $PD1^+$ $CD8^+$ T cells in mice, suggesting that EZH2 may be involved in T cell exhaustion regulation, thereby enhancing antitumor immunity (Fig. 8G). Consistently, shRNA-mediated knockdown of EZH2 or pharmacological inhibition with SHR2554 in mouse HCC cell led to a marked reduction in MIF mRNA and protein levels, indicating a positive association between EZH2 activity and MIF expression (Supplementary Fig. 4).

Further analysis revealed that treatment with the EZH2 inhibitor led to a significant downregulation of EZH2 and MIF expression in murine liver cancer tumors. Additionally, Ki67, a proliferation marker, was also markedly decreased in the SHR2554-treated group (Fig. 8H, I). Using TCGA liver cancer datasets, we found a positive correlation between EZH2 and MIF mRNA expression levels ($R = 0.25$, $P < 0.0001$) (Fig. 8J). Similarly, immunohistochemical analysis of murine subcutaneous tumors confirmed a positive correlation between EZH2 and MIF expression ($R = 0.67$, $P = 0.034$) (Fig. 8K). Furthermore, immunofluorescence analysis showed that SHR2554 treatment led to decreased CD74 expression and increased $CD8^+$ T cell infiltration (Fig. 8L). Taken together, these findings suggest that EZH2 may regulate $CD8^+$ T cell activation and exhaustion through the

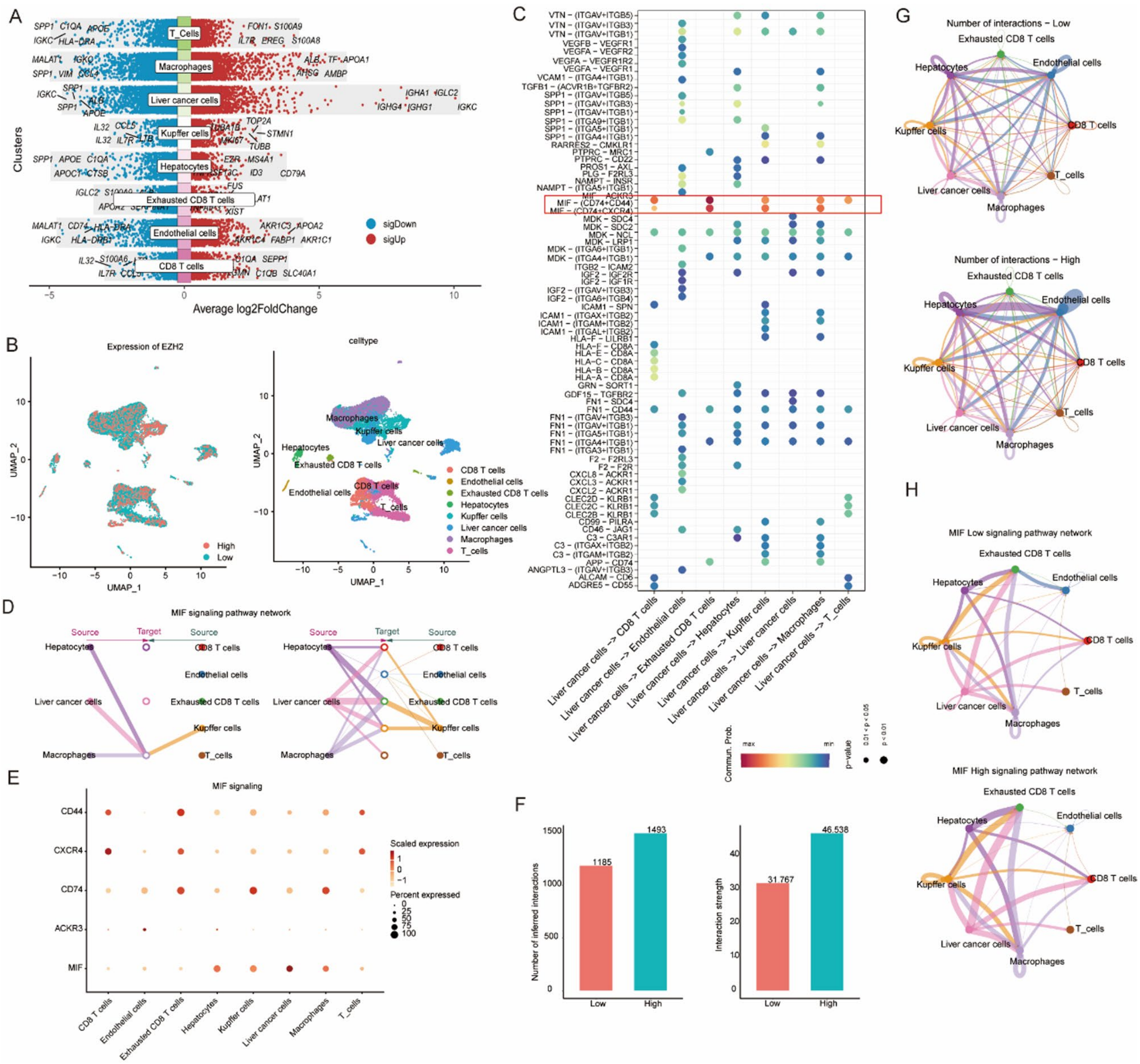

Fig. 7 The role of EZH2 in liver cancer. **A** Based on the median expression of EZH2, cells are divided into high-expression and low-expression EZH2 groups. The scRNA cluster volcano plot shows differential gene expression analysis, displaying upregulated and downregulated genes in all 8 cell types. |log2Fold change| >0.25, p value < 0.05. **B** UMAP plot displaying the distribution of high and low expression of EZH2 across the 8 cell types. **C** Bubble plot showing the ligand-receptor interactions based on Cellchat. The x-axis represents the direction of interaction between different cells, and the y-axis represents specific ligand-receptor pairs. The color of the circles represents the communication probability, and the size of the circles represents the significance of the communication (*p*-value). **D** Hierarchy plot split into two parts: the left half shows autocrine and/or paracrine signaling of hepatocytes, liver cancer cells, and macrophages; the right half displays autocrine and/or paracrine signaling of CD8 T cells, endothelial cells, exhausted CD8 T cells, Kupffer cells, and T cells. The source cell types are shown as solid circles, and target cell types are shown as hollow circles. The left side of the plot positions the target for hepatocytes, liver cancer cells, and macrophages in the middle, illustrating the effects of different cell types on these three cell types. The right side positions the target for CD8 T cells, endothelial cells, exhausted CD8 T cells, Kupffer cells, and T cells, showing the effects of different cell types on these target cell types. The line thickness indicates the strength of interaction. **E** Dot plot displaying the expression of key genes involved in the MIF signaling pathway across different cell types. The size of the bubbles represents the proportion of cells expressing the gene, and the color spectrum represents the average expression level of the marker gene. **F** Bar plot comparing the number of interactions and interaction strength/weight between high and low EZH2 expression cells (with high expression > median and low expression ≤ median). **G**, **H** Circle plot showing the number of interactions (**G**) and interaction strength/weight (**H**) between cell types in the tumor microenvironment for high and low EZH2 expression groups. The color and width of the lines represent the quantity and strength of interactions between different cell types. **I** Dot plot analyzing the strength of signal reception and output across different cell types in the high and low EZH2 expression groups

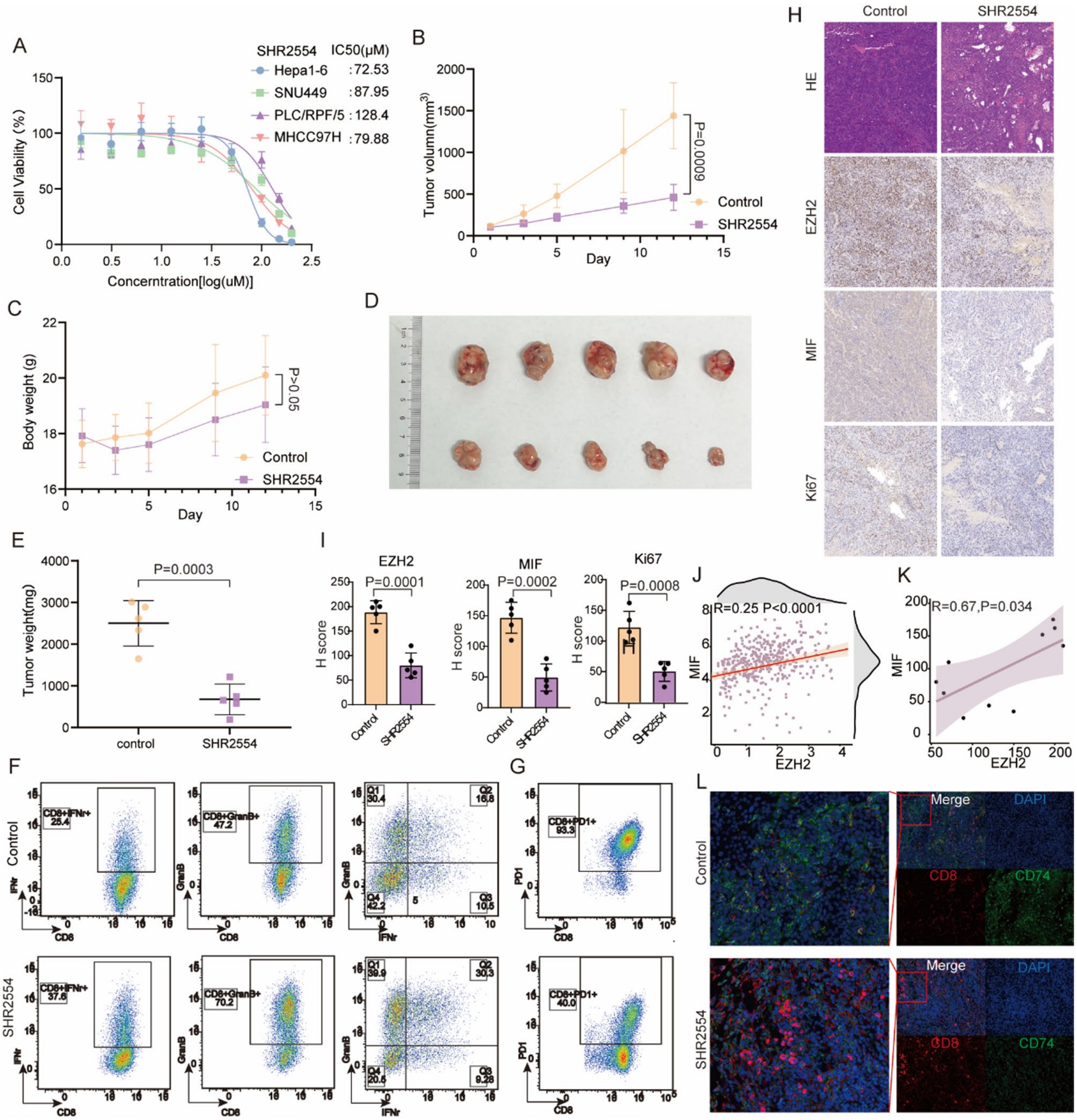

Fig. 8 EZH2 may regulate CD8$^+$ T cell activation and exhaustion via the MIF-CD74 pathway. **A** CCK8 assay showing the sensitivity of human liver cancer cells (SNU449, PLC/PRF/5, MHCC7H) and mouse liver cancer cells (Hepa1-6) to the EZH2 inhibitor SHR2554. **B** Subcutaneous tumor volume in the control group and SHR2554-treated group. **C** Body weight of mice with Hepa1-6 subcutaneous tumor models. **D** Tumor images of subcutaneous tumors in the control and SHR2554-treated groups. **E** Tumor weight of subcutaneous tumors in the control and SHR2554-treated groups. **F** Flow cytometry analysis of the frequency of IFN-γ$^+$ and GranB$^+$ CD8$^+$ T cells in subcutaneous tumors of control and SHR2554-treated mice. **G** Flow cytometry analysis of the frequency of PD1$^+$ CD8$^+$ T cells in subcutaneous tumors of control and SHR2554-treated mice. **H**, **I** Immunohistochemistry showing the changes in EZH2, MIF, and Ki67 protein expression levels in mouse subcutaneous tumors under SHR2554 treatment. **J** Correlation between MIF and EZH2 mRNA levels in TCGA liver cancer data. **K** Immunohistochemical analysis of mouse subcutaneous tumors showing the correlation between MIF and EZH2 mRNA levels. The x-axis and y-axis represent the H score of protein expression. **L** Immunofluorescence analysis of CD8 and CD74 expression in control and SHR2554-treated groups

MIF-CD74 axis, thereby shaping the tumor immune microenvironment.

Discussion

The relationship between dormancy, mitochondrial function, autophagy, senescence, and tumor stemness is intricate and contributes to the malignant phenotype of tumors. It has been reported that mitochondria, through autophagy-mediated degradation, induce a dormant state in subpopulations of cancer cells, granting them resistance to lethal cisplatin exposure. Targeting mitochondrial autophagy may offer a promising strategy to overcome chemoresistance in head and neck squamous cell carcinoma [36]. Mitochondria play a pivotal role in determining the functionality and fate of tumor liver cells, exhibiting distinct characteristics in terms of morphology, subcellular localization, mitochondrial DNA, metabolic status, and mitochondrial autophagic activity [37]. Mitochondrial dysfunction and cellular senescence are hallmarks of aging and are closely related. Damaged mitochondria, along with inefficient oxidative phosphorylation, generate excessive ROS. Increased oxidative stress leads to DNA damage, such as base oxidation, single-strand breaks, double-strand breaks, and telomere shortening, activating p53 and pRb pathways, resulting in cell cycle arrest and senescence [38]. Cellular senescence is established and maintained through mechanisms including excessive ROS production, impaired mitochondrial dynamics, defects in the electron transport chain, bioenergetic imbalance, increased AMPK activity, decreased mitochondrial NAD^+, and metabolic alterations, which disrupt mitochondrial homeostasis and promote the onset and persistence of cellular senescence [39]. Integrating these tumor characteristics may better predict tumor status. By developing and comparing prognostic gene features derived from mitochondria, autophagy, and other relevant genes or comparing with previously published liver cancer RNA-seq data, we found that the combined model offers improved prognostic prediction. Therefore, the comprehensive analysis of multiple models represents a promising strategy for developing accurate tumor prediction models.

The combination of the PD-L1 inhibitor atezolizumab and the anti-angiogenesis drug bevacizumab has become a first-line treatment for advanced HCC. Although this combination therapy outperforms immune checkpoint inhibitors alone and tyrosine kinase inhibitors alone in the treatment of advanced liver cancer, the overall objective response rate of this regimen is only 33.2% [6]. Due to the limited efficacy and response rates of immune inhibitors in liver cancer, scientists have been working to develop accurate biomarkers to predict the efficacy of immunotherapeutics, such as tumor mutational burden (TMB), microsatellite instability (MSI), and PD-L1 expression. However, in liver cancer, TMB is often low, and hypermutation is rare [40], making it inaccurate in predicting the efficacy of immune checkpoint inhibitors [41]. The incidence of MSI-H in liver cancer is also low [42], and the expression of PD-L1 does not always correlate directly with clinical outcomes [43]. The immune microenvironment of liver cancer is very complex, and some liver cancers may respond well to immune checkpoint inhibitors even with low PD-L1 expression. These biomarkers have certain limitations in predicting the outcomes of immunotherapy for liver cancer. Our combined model has preliminarily shown great potential in predicting liver cancer's response to immune inhibitors, but further validation in a larger sample size is needed.

CNV gains and losses can significantly affect tumor behavior and immune response by altering the expression of oncogenes, tumor suppressors, and immune regulatory genes. In our study, nine genes (e.g., EZH2, HSP90AB1, FANCD2, BMI1) exhibited a higher frequency of CNV gains. These genes are involved in oncogenic processes such as chromatin remodeling (EZH2, BMI1), DNA damage repair (FANCD2), and protein folding/chaperone activity (HSP90AB1), all of which contribute to tumor proliferation, genomic instability, and immune evasion. For example: EZH2 orchestrates the regulation of the innate and adaptive immune systems of the tumor microenvironment (TME). Profound epigenetic and transcriptomic changes induced by EZH2 in tumor cells and immune cells mobilize the elements of the TME, leading to immune-suppressive activity of solid tumors [44]. HSP90AB1, as a chaperone protein, stabilizes multiple oncogenic proteins, and its overexpression has been linked to resistance to immune checkpoint inhibitors [45]. Conversely, seven genes (e.g., RELA, GOT2, MUTYH, HSPA8) showed a higher frequency of CNV losses. These genes participate in immune signaling (RELA/NF-κB pathway), metabolic regulation (GOT2), and oxidative DNA repair (MUTYH). Specifically, GOT2 loss might affect other cells in the microenvironment, including immune cells, to directly or indirectly affect tumor growth. Other metabolic enzymes could similarly influence the proliferation or function of various cell types in tumors by affecting environmental nutrient levels [46]. These CNV-driven alterations may partly explain differences in patient prognosis and immunotherapy response.

We also constructed a nomogram incorporating the integrated risk score along with clinical and pathological features in the study cohort. Our nomogram may assist clinicians in tailoring treatment strategies by identifying patients at high risk of poor prognosis, who may benefit from intensified therapy or enrollment in immunotherapy trials, thereby promoting personalized HCC management.

The application of single-cell sequencing has deepened our understanding of the roles of genes in the combined model within liver cancer cells and the tumor microenvironment. In 2019, a study by the team of Zemin Zhang, which combined 10x Genomics and SMART-seq2 single-cell RNA sequencing technologies, revealed the dynamic migration and state transition of immune cells within the liver cancer tumor environment. It analyzed the different lineages and migration relationships of myeloid cells and lymphocytes in the tumor microenvironment, lymph nodes, and ascites, suggesting new possibilities for liver cancer treatment through the modulation of the immune microenvironment [47]. In 2020, Sun Y, et al. systematically presented the differences in the immune microenvironment between primary liver cancer tumors and early recurrent tumors using single-cell transcriptomics, unveiling the characteristic immune signatures and immune evasion mechanisms of early recurrent liver cancer, which provided a theoretical foundation and new ideas for targeting liver cancer's immune microenvironment as a therapeutic strategy [48]. A study discovered a type of tumor-associated macrophages with high expression of platelet-activating factor acetylhydrolase (PLA2G7) in the liver cancer microenvironment, and inhibiting PLA2G7 could improve the immune microenvironment, thereby enhancing the efficacy of HCC immunotherapy [49]. The advancements in single-cell sequencing and bioinformatics have had a positive impact on cancer treatment. By utilizing two single-cell datasets, we uncovered the complex cellular communication network within the liver cancer tumor microenvironment, providing theoretical support for the development of immune-based therapeutic strategies.

Through the development of single-cell trajectory analysis, we revealed the relationship between gene expression changes, such as those of EZH2 and HSPA8, and cell fate determination. To further confirm that EZH2 regulates CD8$^+$ T cell activation and exhaustion through MIF, we constructed a liver cancer xenograft model in immunocompetent mice and applied an EZH2 inhibitor. Our findings suggest that, following the use of the EZH2 inhibitor, the MIF signaling axis may inhibit exhausted CD8$^+$ T cells via CD74, enhancing CD8$^+$ T cell activation and suppressing tumor cells. Currently, only in liver cancer, miR-144/miR-451a has been reported to target MIF, promoting macrophage M1 polarization and anti-tumor activity. The miR-144/miR-451a cluster forms a feedback loop with EZH2 (the catalytic subunit of PRC2) [50]. However, the regulatory relationship between EZH2 and MIF has not been detailed in liver cancer or other tumors. The pro-inflammatory cytokine MIF, along with its ligand CD74, has been studied as a prognostic marker for various cancers, though the results are sometimes contradictory due to differences in cancer types and biomarker detection methods (serum, tumor samples, mRNA, or proteins) [51–53]. In brain tumors, MIF secreted by CD74 activation escapes immune stimulation and promotes the conversion of macrophages from M1 to M2 phenotype. The MIF-CD74 signaling pathway inhibits macrophage secretion of interferon (IFN)-γ through the phosphorylation of ERK1/2. Inhibition of the MIF signaling pathway or its receptor CD74 promotes the release of IFN-γ, enhancing tumor cell death through drug inhibition or siRNA-mediated knockdown [54]. Through single-cell sequencing, Wang et al. discovered that in patients with squamous cell carcinoma of the lung associated with chronic obstructive pulmonary disease, the proportion of tumor-associated macrophages (TAMs) was increased, and the molecular level of CD8$^+$ T cell exhaustion was elevated, leading to an immunosuppressive microenvironment. In these patients, a key CD74$^+$ tumor cell cluster was identified, exhibiting both epithelial and immune cell characteristics, and showing a stronger tumorigenic capacity, which predicted poorer overall survival. One study further revealed that MIF-CD74 might interact with CD8$^+$ T cells and suppress their anti-tumor activity by modulating the PI3K-STAT3-PD-L1 signaling pathway, thereby promoting tumor proliferation and immune escape. Tumor growth was inhibited in C57BL/6 mice with CD74 knockout, but no such effect was observed in immunodeficient mice, suggesting that CD74 may exert its effect through interactions with T cells [55]. In our study, CD8$^+$ T cells in hepatocellular carcinoma (HCC) were primarily in an initial or exhausted state, characterized by decreased expression of cytotoxic factors (such as IFN-γ and GranB) and increased expression of exhaustion markers (such as PD-1). Inhibition of EZH2 may potentially shift T cells to an immune-promoting phenotype through the MIF-CD74 signaling axis. This discovery could provide a novel strategy to enhance the response rate of liver cancer to immune checkpoint inhibitors, addressing the low response rates typically seen in such treatments. Future research will further investigate how MIF-CD74 regulates T cell activity through other key molecules.

Although EZH2 and MIF show a positive correlation in expression ($R = 0.25$), current literature does not support a direct transcriptional regulatory relationship (Fig. 8J). EZH2 may influence MIF expression indirectly through modulation of intermediate inflammatory signaling pathways, such as NF-κB or STAT3, which have been implicated in MIF transcriptional regulation [56, 57]. We agree that further mechanistic studies (e.g., ChIP-seq or CRISPR perturbation) are needed to clarify this relationship.

Despite the integrative nature of our study combining bulk transcriptomic, single-cell, and animal model data, several limitations should be acknowledged. First, while we identified EZH2 as a key regulator associated with CD8$^+$ T cell exhaustion and poor prognosis, the mechanistic link to the MIF-CD74 signaling axis remains largely correlative. We did not perform direct experimental validation such as chromatin immunoprecipitation (ChIP), promoter assays, or in vitro gene perturbation studies to confirm the regulatory relationship. Second, although the murine subcutaneous tumor model provides supportive evidence of immune modulation by EZH2, orthotopic or immunotherapy-treated models may better recapitulate the liver tumor microenvironment. In future work, we plan to perform CRISPR-based EZH2 knockdown and CD74 blockade experiments, combined with immune profiling, to verify the causal role of this axis in modulating CD8$^+$ T cell function and therapeutic response in HCC.

In conclusion, the integrated model effectively predicts the prognosis of liver cancer and the response to immune checkpoint inhibitors. Moreover, EZH2 may influence CD8$^+$ T cell activation and exhaustion through the MIF-CD74 signaling pathway, providing potential biomarkers for selecting suitable patients for immune checkpoint inhibitors and offering therapeutic strategies to overcome low responsiveness to immunotherapy.

Supplementary Information

The online version contains supplementary material available at https://doi.org/10.1186/s12967-025-07071-4.

Supplementary Material 1.

Supplementary Material 2.

Supplementary Material 3.

Acknowledgements
The authors wish to thank the technical support from core facility of basic medical sciences in Shanghai Jiao Tong University School of Medicine.

Author contributions

Y.Z. and Y.X. performed flow cytometry analysis, conducted animal experiment, wrote the main manuscript and prepared Figs. 1, 2, 3 and 8 and M.Y. prepared Fig. 4, Y.Z. performed statistical analysis, J.X. and D.C. prepared Fig. 5 and Supplementary figures, A.W.A. and A.R.A prepared Figs. 6 and 7 and modified the language, C.P. and X.Y. collected data, and prepared Supplementary figures, Y.X. prepared Tables, Z.S. supervised the experimental process and revised the manuscript. All authors reviewed the manuscript.

Funding
This work was funded by grant from the National Natural Science Foundation of China (81772521), National key research and development program of China (2023YFC2411405).

Data availability

Data is provided within the manuscript or supplementary information files.

Declarations

Ethics approval and consent to participate

All animal experiments were carried out according to the institutional guidelines and approved by Animal Care and Use Committee (IACUC) in Shanghai Yishang Biotechnology Co., Ltd. (IACUC-2024-Mi-070).

Consent for publication

Not applicable.

Competing interests

The authors declare no competing interests.

Author details
[1]Department of Oncology, Shanghai Sixth People's Hospital Affiliated to Shanghai JiaoTong University School of Medicine, Shanghai 200030, China
[2]Department of Hematology and Medical Oncology, The Second Affiliated Hospital &Yuying Children's Hospital of Wenzhou Medical University, Wenzhou, China
[3]Department of Infectious Disease, The Second Affiliated Hospital and Yuying Children's Hospital of Wenzhou Medical University, Wenzhou, China

Received: 28 May 2025 / Accepted: 31 August 2025

References

1. Vogel A, Meyer T, Sapisochin G, Salem R, Saborowski A. Hepatocellular carcinoma. Lancet. 2022;400(10360):1345–62.
2. Yang X, Yang C, Zhang S, Geng H, Zhu AX, Bernards R, Qin W, Fan J, Wang C, Gao Q. Precision treatment in advanced hepatocellular carcinoma. Cancer Cell. 2024;42(2):180–97.
3. Galle PR, Dufour JF, Peck-Radosavljevic M, Trojan J, Vogel A. Systemic therapy of advanced hepatocellular carcinoma. Future Oncol. 2021;17(10):1237–51.
4. Jin H, Shi Y, Lv Y, Yuan S, Ramirez CFA, Lieftink C, Wang L, Wang S, Wang C, Dias MH, et al. EGFR activation limits the response of liver cancer to lenvatinib. Nature. 2021;595(7869):730–4.
5. Finn RS, Qin S, Ikeda M, Galle PR, Ducreux M, Kim TY, Kudo M, Breder V, Merle P, Kaseb AO, et al. Atezolizumab plus bevacizumab in unresectable hepatocellular carcinoma. N Engl J Med. 2020;382(20):1894–905.
6. Rizzo A, Ricci AD, Brandi G. Atezolizumab in advanced hepatocellular carcinoma: good things come to those who wait. Immunotherapy. 2021;13(8):637–44.
7. Chun Y, Kim J. Autophagy: an essential degradation program for cellular homeostasis and life. Cells-Basel. 2018;7(12).
8. Li X, He S, Ma B. Autophagy and autophagy-related proteins in cancer. Mol Cancer. 2020;19(1):12.
9. Sharif T, Martell E, Dai C, Kennedy BE, Murphy P, Clements DR, Kim Y, Lee PW, Gujar SA. Autophagic homeostasis is required for the pluripotency of cancer stem cells. Autophagy. 2017;13(2):264–84.
10. Smith AG, Macleod KF. Autophagy, cancer stem cells and drug resistance. J Pathol. 2019;247(5):708–18.
11. Nazio F, Bordi M, Cianfanelli V, Locatelli F, Cecconi F. Autophagy and cancer stem cells: molecular mechanisms and therapeutic applications. Cell Death Differ. 2019;26(4):690–702.
12. Childs BG, Durik M, Baker DJ, van Deursen JM. Cellular senescence in aging and age-related disease: from mechanisms to therapy. Nat Med. 2015;21(12):1424–35.
13. Kuilman T, Michaloglou C, Mooi WJ, Peeper DS. The essence of senescence. Genes Dev. 2010;24(22):2463–79.
14. Leontieva OV, Blagosklonny MV. CDK4/6-inhibiting drug substitutes for p21 and p16 in senescence: duration of cell cycle arrest and MTOR activity determine geroconversion. Cell Cycle. 2013;12(18):3063–9.
15. Gewirtz DA. Autophagy and senescence: a partnership in search of definition. Autophagy. 2013;9(5):808–12.
16. Rubinsztein DC, Gestwicki JE, Murphy LO, Klionsky DJ. Potential therapeutic applications of autophagy. Nat Rev Drug Discov. 2007;6(4):304–12.
17. Levine B, Kroemer G. Autophagy in the pathogenesis of disease. Cell. 2008;132(1):27–42.
18. Liu R, Zhao Y, Su S, Kwabil A, Njoku PC, Yu H, Li X. Unveiling cancer dormancy: intrinsic mechanisms and extrinsic forces. Cancer Lett. 2024;591:216899.
19. Min HY, Lee HY. Cellular dormancy in cancer: mechanisms and potential targeting strategies. Cancer Res Treat. 2023;55(3):720–36.
20. DeLuca VJ, Saleh T. Insights into the role of senescence in tumor dormancy: mechanisms and applications. Cancer Metastasis Rev. 2023;42(1):19–35.

21. Akkoc Y, Gozuacik D. Autophagy and hepatic tumor microenvironment associated dormancy. J Gastrointest Cancer. 2021;52(4):1277–93.
22. Hwang B, Lee JH, Bang D. Single-cell RNA sequencing technologies and bioinformatics pipelines. Exp Mol Med. 2018;50(8):1–14.
23. Zhang Y, Chen H, Mo H, Hu X, Gao R, Zhao Y, Liu B, Niu L, Sun X, Yu X, et al. Single-cell analyses reveal key immune cell subsets associated with response to PD-L1 Blockade in triple-negative breast cancer. Cancer Cell. 2021;39(12):1578–93. e1578.
24. Hirz T, Mei S, Sarkar H, Kfoury Y, Wu S, Verhoeven BM, Subtelny AO, Zlatev DV, Wszolek MW, Salari K, et al. Dissecting the immune suppressive human prostate tumor microenvironment via integrated single-cell and Spatial transcriptomic analyses. Nat Commun. 2023;14(1):663.
25. Meng Y, Zhao Q, An L, Jiao S, Li R, Sang Y, Liao J, Nie P, Wen F, Ju J, et al. A TNFR2-hnRNPK axis promotes primary liver cancer development via activation of YAP signaling in hepatic progenitor cells. Cancer Res. 2021;81(11):3036–50.
26. Ma L, Hernandez MO, Zhao Y, Mehta M, Tran B, Kelly M, Rae Z, Hernandez JM, Davis JL, Martin SP, et al. Tumor cell biodiversity drives microenvironmental reprogramming in liver cancer. Cancer Cell. 2019;36(4):418–e430416.
27. Mizushima N, Komatsu M. Autophagy: renovation of cells and tissues. Cell. 2011;147(4):728–41.
28. Levine B, Kroemer G. Biological functions of autophagy genes: a disease perspective. Cell. 2019;176(1–2):11–42.
29. Rath S, Sharma R, Gupta R, Ast T, Chan C, Durham TJ, Goodman RP, Grabarek Z, Haas ME, Hung WHW, et al. MitoCarta3.0: an updated mitochondrial proteome now with sub-organelle localization and pathway annotations. Nucleic Acids Res. 2021;49(D1):D1541–7.
30. Tacutu R, Thornton D, Johnson E, Budovsky A, Barardo D, Craig T, Diana E, Lehmann G, Toren D, Wang J, et al. Human ageing genomic resources: new and updated databases. Nucleic Acids Res. 2018;46(D1):D1083–90.
31. Yang J, Xu H, Li C, Li Z, Hu Z. An explorative study for leveraging transcriptomic data of embryonic stem cells in mining cancer stemness genes, regulators, and networks. Math Biosci Eng. 2022;19(12):13949–66.
32. Zhu Q, Yang Y, Chen K, Zhang Q, Huang Y, Jian S. Diffuse large B-cell lymphoma: the significance of CD8(+) tumor-infiltrating lymphocytes exhaustion mediated by TIM3/Galectin-9 pathway. J Transl Med. 2024;22(1):174.
33. Fu J, Li K, Zhang W, Wan C, Zhang J, Jiang P, Liu XS. Large-scale public data reuse to model immunotherapy response and resistance. Genome Med. 2020;12(1):21.
34. Xu B, Lu M, Yan L, Ge M, Ren Y, Wang R, Shu Y, Hou L, Guo H. A pan-cancer analysis of predictive methylation signatures of response to cancer immunotherapy. Front Immunol. 2021;12:796647.
35. Jiang P, Gu S, Pan D, Fu J, Sahu A, Hu X, Li Z, Traugh N, Bu X, Li B, et al. Signatures of T cell dysfunction and exclusion predict cancer immunotherapy response. Nat Med. 2018;24(10):1550–8.
36. Sun Y, Chen Y, Liu Z, Wang J, Bai J, Du R, Long M, Shang Z. Mitophagy-mediated tumor dormancy protects cancer cells from chemotherapy. Biomedicines. 2024;12(2).
37. Zheng XX, Chen JJ, Sun YB, Chen TQ, Wang J, Yu SC. Mitochondria in cancer stem cells: achilles heel or hard armor. Trends Cell Biol. 2023;33(8):708–27.
38. Miwa S, Kashyap S, Chini E, von Zglinicki T. Mitochondrial dysfunction in cell senescence and aging. J Clin Invest. 2022;32(13).
39. Abate M, Festa A, Falco M, Lombardi A, Luce A, Grimaldi A, Zappavigna S, Sperlongano P, Irace C, Caraglia M, et al. Mitochondria as playmakers of apoptosis, autophagy and senescence. Semin Cell Dev Biol. 2020;98:139–53.
40. Ang C, Klempner SJ, Ali SM, Madison R, Ross JS, Severson EA, Fabrizio D, Goodman A, Kurzrock R, Suh J, et al. Prevalence of established and emerging biomarkers of immune checkpoint inhibitor response in advanced hepatocellular carcinoma. Oncotarget. 2019;10(40):4018–25.
41. Yang H, Sun L, Guan A, Yin H, Liu M, Mao X, Xu H, Zhao H, Lu X, Sang X, et al. Unique TP53 neoantigen and the immune microenvironment in long-term survivors of hepatocellular carcinoma. Cancer Immunol Immunother. 2021;70(3):667–77.
42. Terashima T. Microsatellite instability-high in Japanese patients with hepatocellular carcinoma. Hepatol Res. 2020;50(7):773–4.
43. Zhu AX, Finn RS, Edeline J, Cattan S, Ogasawara S, Palmer D, Verslype C, Zagonel V, Fartoux L, Vogel A, et al. Pembrolizumab in patients with advanced hepatocellular carcinoma previously treated with Sorafenib (KEYNOTE-224): a non-randomised, open-label phase 2 trial. Lancet Oncol. 2018;19(7):940–52.
44. Sun S, Yu F, Xu D, Zheng H, Li M. EZH2, a prominent orchestrator of genetic and epigenetic regulation of solid tumor microenvironment and immunotherapy. Biochim Biophys Acta Rev Cancer. 2022;1877(2):188700.
45. Mbofung RM, McKenzie JA, Malu S, Zhang M, Peng W, Liu C, Kuiatse I, Tieu T, Williams L, Devi S, et al. HSP90 Inhibition enhances cancer immunotherapy by upregulating interferon response genes. Nat Commun. 2017;8(1):451.
46. Do BT, Vander Heiden MG. GOT2 consider the tumor microenvironment. Trends Cancer. 2022;8(11):884–6.
47. Zhang Q, He Y, Luo N, Patel SJ, Han Y, Gao R, Modak M, Carotta S, Haslinger C, Kind D, et al. Landscape and dynamics of single immune cells in hepatocellular carcinoma. Cell. 2019;179(4):829–e845820.
48. Sun Y, Wu L, Zhong Y, Zhou K, Hou Y, Wang Z, Zhang Z, Xie J, Wang C, Chen D, et al. Single-cell landscape of the ecosystem in early-relapse hepatocellular carcinoma. Cell. 2021;184(2):404–21.
49. Zhang F, Liu W, Meng F, Jiang Q, Tang W, Liu Z, Lin X, Xue R, Zhang S, Dong L. Inhibiting PLA2G7 reverses the immunosuppressive function of intratumoral macrophages and augments immunotherapy response in hepatocellular carcinoma. J Immunother Cancer. 2024;12(1).
50. Zhao J, Li H, Zhao S, Wang E, Zhu J, Feng D, Zhu Y, Dou W, Fan Q, Hu J, et al. Epigenetic Silencing of miR-144/451a cluster contributes to HCC progression via paracrine HGF/MIF-mediated TAM remodeling. Mol Cancer. 2021;20(1):46.
51. Noer JB, Talman MM, Moreira JMA. HLA Class II Histocompatibility Antigen gamma Chain (CD74) Expression Is Associated with Immune Cell Infiltration and Favorable Outcome in Breast Cancer. Cancers (Basel). 2021;13(24).
52. Ekmekcioglu S, Davies MA, Tanese K, Roszik J, Shin-Sim M, Bassett RL Jr., Milton DR, Woodman SE, Prieto VG, Gershenwald JE, et al. Inflammatory marker testing identifies CD74 expression in melanoma tumor cells, and its expression associates with favorable survival for stage III melanoma. Clin Cancer Res. 2016;22(12):3016–24.
53. Xu S, Li X, Tang L, Liu Z, Yang K, Cheng Q. CD74 correlated with malignancies and immune microenvironment in gliomas. Front Mol Biosci. 2021;8:706949.
54. Ghoochani A, Schwarz MA, Yakubov E, Engelhorn T, Doerfler A, Buchfelder M, Bucala R, Savaskan NE, Eyupoglu IY. MIF-CD74 signaling impedes microglial M1 polarization and facilitates brain tumorigenesis. Oncogene. 2016;35(48):6246–61.
55. Wang D, Li S, Yang Z, Yu C, Wu P, Yang Y, Zhang R, Li Q, Yang J, Li H, et al. Single-cell transcriptome analysis Deciphers the CD74-mediated immune evasion and tumour growth in lung squamous cell carcinoma with chronic obstructive pulmonary disease. Clin Transl Med. 2024;14(8):e1786.
56. Kaur P, Verma S, Kushwaha PP, Gupta S. EZH2 and NF-kappaB: a context-dependent crosstalk and transcriptional regulation in cancer. Cancer Lett. 2023;560:216143.
57. Liu Z, Li Z, Yan G, Lin C, Luo Y, Ye Y, Zeng X, Yao J. MIF promotes Th17 cell differentiation in hashimoto's thyroiditis by binding HVEM and activating NF-kappaB signaling pathway. Int Immunopharmacol. 2023;121:110494.

Publisher's note